Article

Full Dynamics Description of Mg Phthalocyanine Crystalline and Amorphous Semiconductor Systems

D. Potamianos, M. Nuber, A. Schletter, M. Schnitzenbaumer, M. Haimerl, P. Scigalla, M. Wörle, L. I. Wagner, R. Kienberger,* and H. Iglev*

Read Online

ACCESS | Metrics & More | Article Recommendations | Supporting Information

ABSTRACT: Based on visible and mid-infrared transient absorption studies, probing the inter- and intraband dynamics, respectively, of magnesium phthalocyanine (MgPc) organic semiconductors, we were able to develop a model to describe the dynamics and the resulting optical response. We demonstrate how the model could offer insights into the dynamics of more complicated systems such as amorphous MgPc samples obtained by established preparation methods. In particular, we show a clear dimensionality difference of the exciton dissipation mechanism between crystalline and amorphous MgPc, which we resolve in the intraband dynamics, and how this result can also be deduced from the interband dynamics through the implementation of the developed model.
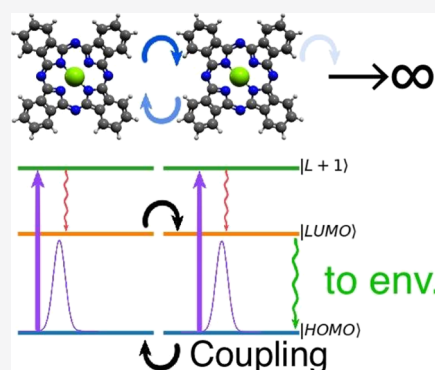
INTRODUCTION

Phthalocyanine (Pc) derivatives make up a diverse group of great interest, not only due to the similarity with compounds found in the nature, such as chlorophyll, porphyrins, and hemoglobin, but also because they can host a number of metal atoms or even metal-containing groups. Pc derivatives tend to be chemically, thermally, and optically stable. Their symmetry allows them to form good-quality organic thin-film semi-conductors and even highly organized mono-layers.[1,2] This makes them good candidates for a plethora of applications ranging from catalysts and environment sensing devices[3,4] to organic electronic and opto-electronic devices such as organic thin-film transistors,[5] organic photovoltaics,[6,7] and organic light-emitting diodes.[8]

The most common preparation methods of such films are Langmuir−Blodgett,[9−11] spin-coating,[12,13] and vapor deposition[14,15] methods. Out of the different metal−Pc complexes, magnesium Pc (MgPc) stands out in the sense that the first two preparation methods result in a thin film with an intense and broad near-infrared (NIR) absorption peak centered around 815 nm (Figure 1A, green line),[16,17] which is present neither in the recorded spectra of solutions (Figure 1A, blue line) nor when the film is prepared by the latter preparation method.[18] It has been argued that this absorption peak is caused by the so-called X-phase of MgPc.[18] This structural configuration gives rise to intense exciton coupling effects that cause the observed spectral shift of the Q-band to higher wavelengths.[18] Since the vapor deposition method results in films with absorption spectra that had the greatest similarity to those of solutions of MgPc, it was considered a higher-quality

film. This was because of a lower degree of molecular distortions and a more organized crystal structure, resulting in minimal broadenings and shifts in the molecular bands.[19,20] Therefore, a lot of studies about the optical properties of MgPc and similar derivatives were carried out, mainly prepared by vapor deposition methods, giving insights into the exciton annihilation mechanisms taking place in such samples.[21−26] Nevertheless, all the abovementioned preparation methods result in polycrystalline and amorphous samples.[27,28]

Recently, a new preparation method, namely, liquid deposition, was developed, which is expected to produce single-crystal films.[29] It was then demonstrated by Ran et al.[30] that one can obtain thin MgPc films easily and without the need for extensive setups, as is necessary for vapor deposition. Most importantly, the resulting films were spectrally closer to the solutions than the vapor-deposited ones,[18] which is indicative of the absence of molecular distortions,[31] making it an ideal reference system. In the same study, a comparison between the liquid-deposited film and MgPc dissolved in dichloromethane (DCM) was performed by means of visible-pump visible-probe transient absorption spectroscopy.[30] The two different phases of MgPc were reported to behave almost identically with respect to the fast dynamics. On the other
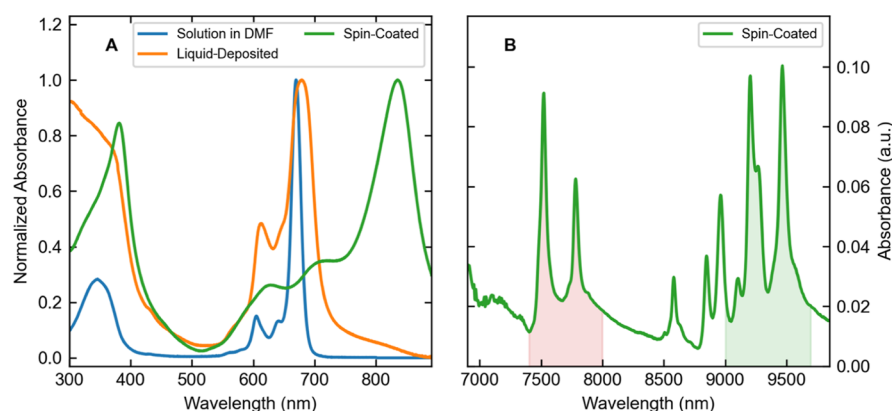
Figure 1. Normalized steady-state UV−vis absorption spectra of MgPc dissolved in DMF and MgPc thin films by different preparation methods (A). Steady-state FTIR spectrum of the spin-coated MgPc film (B) in absorbance units (a.u.). The designated regions (shaded in red and green) correspond to the MIR regions studied in this work.

hand, the long-lived nonradiative energy dissipation mechanisms were very different. The decay mechanism of the solid-phase sample was much faster than the one in the dissolved sample due to the higher interaction of the close-packed MgPc molecules. It is already understood that MgPc molecules tend to π-stack, forming almost one-dimensional columns, allowing for exciton coupling and charge transport along next neighbors.[32]

In the present work, two sets of MgPc thin films were prepared, one set fabricated by liquid deposition and the other by spin-coating. Utilizing pump−probe transient absorption techniques in the mid-infrared (MIR) and visible spectral ranges, we studied the intra- and interband dynamics of both the resulting crystalline and amorphous samples, respectively. A simulation toy model was developed, which offers a simple and accurate description of the crystalline sample's interband dynamics in terms of transitions between three discrete energy levels as well as the exciton interactions and energy dissipation. The amorphous sample's complex behavior could then be analyzed in terms of two independent components: one similar to that of the crystalline sample and one with different optical and excitonic properties.

■ METHODS

Film Fabrication and Characterization. Liquid-deposited samples were manufactured following the process described elsewhere.[30] In our preparation process, a saturated solution (∼0.6 mg/mL) of MgPc in DCM was used instead of the described concentration in order to obtain films with reasonable optical density as it was necessary for conducting the experiments. The films were then transferred to BaF$_2$ or CaF$_2$ optical plates according to the spectral range investigated by MIR transient absorption. A saturated solution of MgPc in N,N-dimethylformamide (DMF) was also used for the fabrication of the spin-coated samples with a homemade spin-coater. BaF$_2$ or CaF$_2$ plates were stabilized on a rotating platform with a rotation speed of approximately 5000 rpm. All samples were characterized using UV−vis spectroscopy. Nominal values for the UV−vis absorbance maximum of the samples depicted in Figure 1A are 1.26 a.u. for the solution in DMF with a concentration of 0.08 mg/mL, 0.45 a.u. for the liquid-deposited sample, and 0.71 a.u. for the spin-coated samples. The fabricated films were also characterized using grazing incidence X-ray diffraction, which ensured the

crystallinity of the liquid-deposited sample and the amorphous nature of the spin-coated sample. For more details, see the Supporting Information.

MIR Transient Absorption Measurements. In order to monitor the intraband dynamics and the vibrational cooling process, we used a visible-pump MIR probe setup based on a Ti/sapphire amplifier (800 nm, 1 kHz, 100 fs). Pump pulses were generated using a noncollinear optical amplifier (NOPA) or the fundamental output of the Ti/sapphire amplifier. The MIR probe pulses were obtained from a two-stage NIR optical parametric amplifier with a subsequent difference-frequency generation in AgGaS$_2$ of the signal and idler pulse. To improve the signal-to-noise ratio, the probe pulses were split into two, with one pulse passing the sample at the excitation position and the other pulse passing at some distance to the pump pulse, allowing referencing. A chopper wheel blocked every second pump beam to determine the absorbance change $[\Delta A = -\log_{10}(T/T_0)]$ upon excitation, with T being the transmittance through the excited sample and T_0 being the reference transmission through the unexcited sample. Both probe beams were recorded on a 2×64-pixel HgCdTe detector after passing a spectrometer. Pump and probe beams had a parallel polarization. To ensure that no anisotropy effects occurred, some measurements were conducted with both parallel and perpendicular polarizations, yielding no relevant differences between the polarizations. Perpendicular polarization data are shown in the Supporting Information (Figures S2 and S3). The pump beam had a focus size (determined by knife's edge method 10/90) of approximately 190 μm for the NOPA beams and of approximately 120 μm for the 800 nm beam. For all transient absorption measurements, multiple scans were averaged to improve the signal-to-noise ratio. Subsequent scans showed no signs of sample degradation.

Visible Transient Absorption Measurements. Transient absorption measurements on the visible range were performed with an experimental setup that is based on a commercial Ti/sapphire laser system, which yields 25 fs pulses with 1.2 mJ at a repetition rate of 3 kHz.[33,34] These are broadened in a hollow core fiber setup filled with neon gas (p = 1.7 bar) and compressed using chirped mirrors to yield few-cycle pulses around 800 nm. A small portion of the beam (30 nJ) is used as a broadband probe, spanning a bandwidth of approximately 550−900 nm. The major part (300 μJ) is doubled in frequency to 400 nm in a thin beta barium borate crystal and serves as a tunable pump with a typically down to

15 fs duration fwhm. A chopper wheel blocks every second pump pulse, which enables highly sensitive pump–probe measurements due to shot-to-shot referencing. Using a variable delay line, the temporal delay between pump and probe pulses could be adjusted. Aiming the best possible temporal resolution, a collinear beam geometry was chosen at the sample. The detection system consists of a home-built polarization-resolved prism spectrometer and a set of CCD detectors each for parallel and perpendicular polarizations of the probe. Here, the perpendicular polarization was used to ensure the highest signal-to-noise ratio. The energy transmittance of the probing pulse through the excited sample was compared to the probe transmittance for the blocked pump beam. As a result, the excitation-induced change of the absorbance was determined for various probe wavelengths and delay steps.

Simulations. Simulations of the results in the visible-probe range were performed by numerically integrating the Lindblad equation to obtain the population of all states of the system for all delay times present in the experiments. A time-dependent perturbation was introduced in the Hamiltonian to describe the exciting pulse, for which an amplitude of 0.54 V/nm, a photon energy of 3.0 eV, and a Gaussian envelope with an FWHM duration of 40 fs were used.

Although it is possible to include an extensive number of states to accurately describe the entire spectral range under consideration, the computational load increases drastically, while no major physical insights would come from such efforts. Thus, simplicity was a requirement in the system's description. Under such conditions, a five-level system was selected as it exhibits enough complexity for both ground-state bleaching (GSB) and excited-state absorption (ESA) to take place. The third and fourth excited states play no active role in the dynamics other than enabling the ESA to manifest. A schematic of the system as it was used for the liquid-deposited sample can be seen in Figure 2, where all the transitions induced by both the MIR- and visible-probe experiments are depicted (the intraband dynamics are presented for clarity but are not described by the model). The eigenenergies of the first two states ($|0>$ and $|1>$) were chosen such that the main absorption peak of the Q-band[35] (or the NIR absorption band

in the case of the amorphous sample) is described accurately. The eigenenergy of the second excited state ($|2>$) was selected such that a representation of the B-band[35] exists and that the exciting radiation is reasonably resonant with the $0 \rightarrow 2$ transition. Lastly, the eigenenergies for the higher excited states ($|3>$ and $|4>$) were selected in accordance to the experimentally measured ESA spectrum. The dipole matrix μ was selected as a matrix of zeros in the diagonal and ones in the off-diagonal elements. It was then optimized to achieve a match of the simulation pump intensity with the measured intensity in the experiment. For modeling the relaxation of the system, two separate mechanisms have to be considered. First, the decay of the states was modeled by including sufficient collapse operators in the Lindblad equation. The only relevant rate for our case was the decay of the second excited state into the first excited state, the value of which was selected to match the experiment. The rest were either irrelevant or had to be set to values higher than the experimental observation window. The second is the excitonic dissipation mechanism. To simulate this mechanism, the model was extended to include two molecules. An interaction Hamiltonian was added in the form of[36]

$$H_{\text{int}} = g(\sigma_1^+ \sigma_2^- + \sigma_1^- \sigma_2^+) \tag{1}$$

where g is the coupling strength between the molecules and σ_k^+ and σ_k^- are the ladder operators for the kth−molecule. This was done to include any exciton effects.[36] Furthermore, another collapse operator was given to include a decay of the second molecule's first excited state. This represents a loss of energy to the environment in a semi-finite chain of molecules due to the molecules at infinity having virtually no energy. The inclusion of both modifications allows the system to decay at a slower rate than what can be achieved by means of collapse operators alone. A major compromise from oversimplifying the excitonic interactions in this model, by reducing the number of molecules down to two, is that the system cannot hold a realistic amount of energy. The coupling strength can be used to match the decay rate, and it is only useful in a comparative study of similar systems. The decay rate defines the time that this mechanism needs in order to take place, and unlike the coupling strength, its value is nearly independent of the number of molecules used in the simulation, which results in having to use a realistic dissipation rate. This is inevitably corrected by reducing the coupling strength to limit the percentage of energy loss to the environment. In turn, if the effect is long-lived, the simulated molecules end up having significant differences in their population distribution, which results in an oscillation of the simulated signal that is not present in the experiment.

A readily available library was used to set up the system and perform the integration of the Lindblad equation.[37,38] Results from such calculations are depicted and discussed in the Supporting Information. Once the density matrix (ρ) was calculated, the population difference was determined, and a spectral component was generated for every possible transition for every delay step. Summing all the spectral components results in a synthesized spectrum for every delay step. The bandwidth given for the spectral width of every peak was 4 THz. A reference spectrum (when the system is on the ground state) was subtracted from all spectra to generate a transient absorption spectrogram. The temporal evolution of the synthesized transient absorption at wavelengths equal to the respective ground- ($|0>$) to first- ($|1>$) excited state and first-
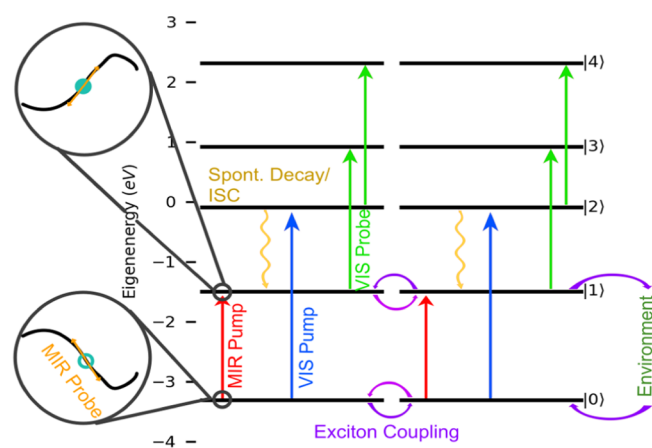

Figure 2. Energy levels and dynamics scheme of the five-level model for the liquid-deposited sample, with the transitions induced by each experiment also shown. The MIR-pump refers to the excitation applied in the MIR transient absorption experiment, while VIS refers to the visible transient absorption experiment.
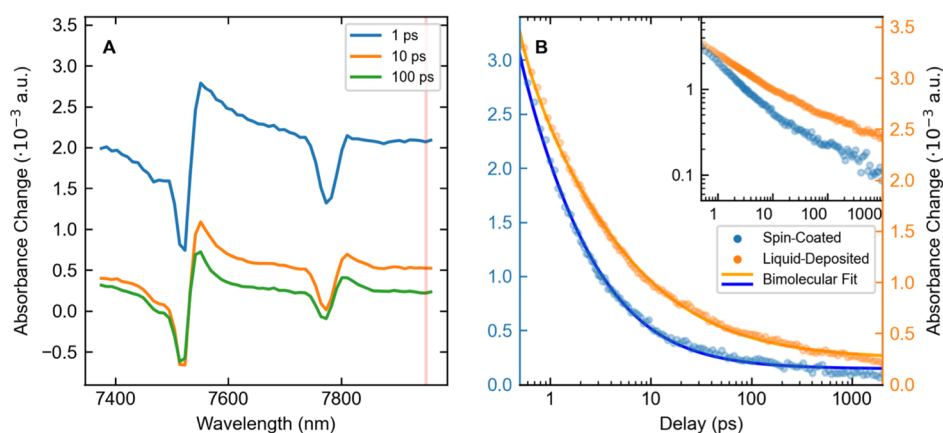
Figure 3. Transient absorption spectra (across the red-designated spectral region of Figure 1B) for the spin-coated sample (A) and the transient absorption signal at 7950 nm (B) for the two solid samples. The inset in the log−log scale highlights the use for a bimolecular fit.

(|1>) to third- (|3>) excited state (which is the same as the second- (|2>) to fourth- (|4>) excited state) transitions were evaluated as the GSB and ESA signal, respectively. The simulated signal intensities were scaled by a multiplication factor to account for the unknown absorption cross-section and the number of molecules on each sample.

RESULTS AND DISCUSSION

The picosecond visible-pump MIR-probe transient absorption spectroscopy setup was deployed as it is sensitive to the intraband transitions[39] taking place in such organic semiconductor materials,[40−43] as well as to molecular vibrations and distortions.[44] Fourier-transform infrared (FTIR) spectra were recorded for the different MgPc films, as seen in Figure 1B. The two samples were pumped to the first excited state by 610 and 800 nm pulses, for the crystalline and amorphous samples, respectively. The region between 7400−8000 and 9000−9700 nm were investigated (red- and green-highlighted regions in Figure 1B, respectively). Typical transient absorption spectra recorded at different delays for the spin-coated (amorphous) sample in the 7400−8000 nm region are depicted in Figure 3A as an example. In all cases and for both samples, two different effects were present. The first observable effect was a red shift in all present absorption peaks, as seen by the characteristic "valley-peak" behavior around the wavelengths, where absorption peaks are observable in the steady-state FTIR spectra. The second effect observed is a uniform absorption increase in the measured spectral range. The red shift was found to be primarily caused by the local transient heating caused by the pump pulse radiation. Comparing the red shifts in our time-resolved experiments with temperature-dependent FTIR measurements, it was possible to deduce a temperature change of a few Kelvins (a more detailed discussion can be found in the Supporting Information, together with Figure S1). The uniform absorption increase, on the other hand, can be assigned to intraband transitions that become available as electron−hole pairs are generated (see also Figure 2).[45] The lack of any characteristic features in the broad absorption indicates the absence of any significant intraband relaxation mechanism as the transient absorption in the entire spectral region decreases in the same way for all wavelengths. Nonetheless, one is able to deduce the rate at which holes in the valence band are being filled by the decay of the excited state. In all cases, the relaxation dynamics were best modeled after a bimolecular excitonic mechanism described as follows[46]

$$\Delta A = A \frac{1}{\frac{N}{n_0} + 2\gamma_0 N t^c} \tag{2}$$

where A relates to the absorption maximum and the extinction coefficients of the molecule in ground and excited states, n_0 is the initial exciton density, N is the molecule density, γ_0 is the initial annihilation constant, and c is a factor related to the dimensionality of exciton motion. In Figure 3B, the absorbance change at 7950 nm is plotted for different delay times for the amorphous (blue points) and crystalline (orange points) samples. The inlay plots present the same data set in a logarithmic scale to highlight the differences. The solid lines represent least-square fits of eq 2 for each sample. A significant difference was found between the two samples mainly in the dimensionality factor c, being 0.62 and 0.85 for the liquid-deposited and spin-coated samples, respectively. This indicates that in the liquid-deposited sample, an almost one-dimensional excitonic dissipation mechanism is taking place, while on the spin-coated sample, there is higher-dimensionality dissipation with no favored diffusion direction.[46]

Knowing the nature of the relaxation dynamics which are dominated by the intermolecular relaxation mechanisms, an investigation in greater depth of the interband dynamics and with better temporal resolution would give further insights into the intramolecular processes. This was achieved by utilizing the femtosecond transient absorption spectroscopy setup using 400 nm pulses for pumping the system and visible broadband pulses (550−900 nm) for probing the state of the system. Figure 4 depicts a set of recorded data for the two different variants of MgPc films. For the crystalline sample (Figure 4A), we observed a broad ESA over the full observation range. Furthermore, for every absorption peak (680 and 610 nm), there is a decrease of the ESA or even inversions of the signal. These are manifestations of GSB, although the signal from the second absorption peak was not strong enough to outdo the ESA. For the case of the amorphous sample (Figure 4B), we observe again a broad ESA signal interrupted two times due to GSB: one around 815 nm and one around 600 nm. A decrease of the ESA around 700 nm is also observed, but the GSB in this spectral region is not that significant for the specific sample. A multi-exponential fitting of the time evolution indicated that all the main contributing effects behave the same across the entire spectral range and are common between ESA and GSB for a given sample. By comparing the transient absorption signal recorded from the two samples (shown in
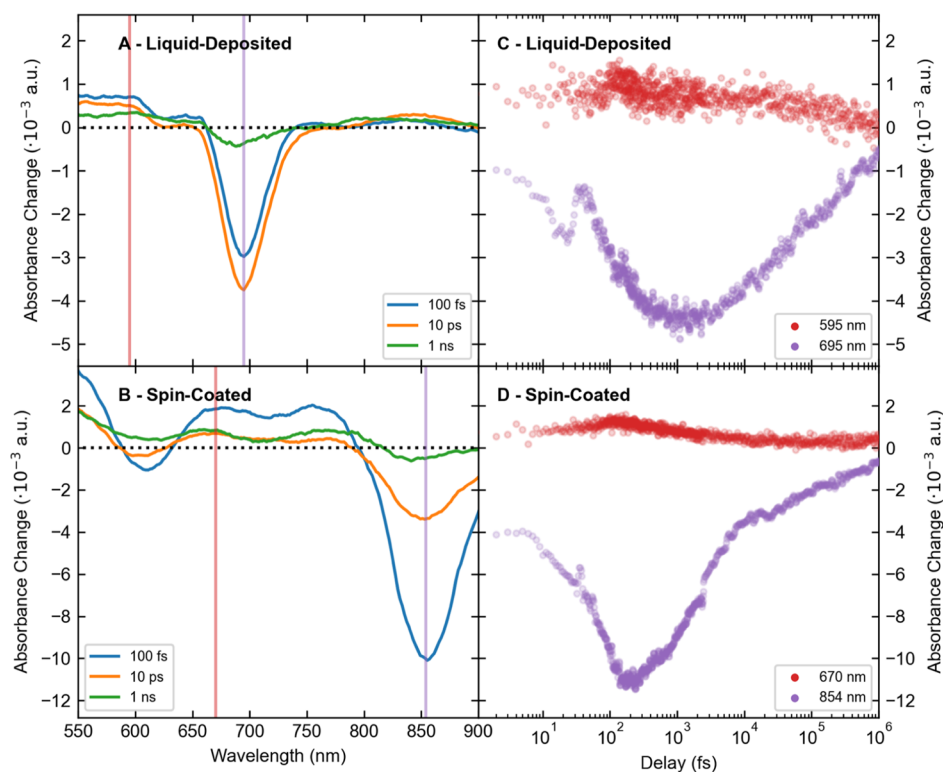
Figure 4. Transient absorption spectra in the visible region recorded for liquid-deposited (A) and spin-coated (B) samples. The vertical lines highlight the regions of averaging for ESA and GSB signals, the time evolutions of which are shown on the right side (C,D).

Figure 4C, D), it is evident that the signal amplitude from the amorphous sample seems to increase faster than the equivalent signal from the crystalline sample and then decreases faster with a time constant in the order of 1 ps. The effect is over within the first 10 ps, and from that point on, the two samples behave almost identically (see green data points in Figure 5).
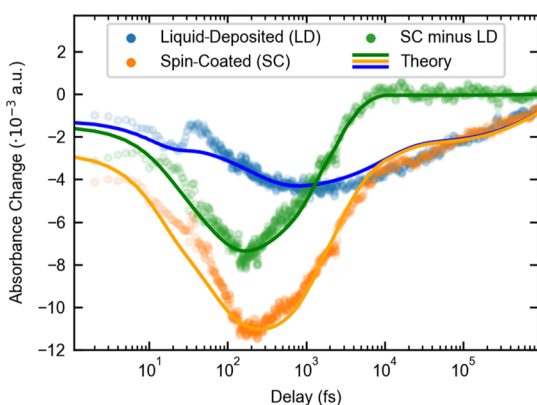

Figure 5. Transient absorption signal as predicted for crystalline MgPc (blue), the amorphous state (orange), and the difference between liquid-deposited and spin-coated films (green). An overlay between the measured data (dots) and the model's prediction (solid lines) for the GSB is presented.

A toy model of the molecule was developed as described above. This gave a solid platform for interpreting the results of the visible-pump visible-probe transient absorption experiment and helped pin the observed signals to a set of transitions and dissipation mechanisms taking place in the samples.

One can derive a good match of the transient absorption signal in the visible range measured in the present study for the crystalline sample, explaining the major spectral features and their temporal evolution in terms of transitions between three states and an excitonic decay mechanism. The pumping transfers population from the ground state to the second excited state (blue arrow in Figure 2). The fast decaying (second excited) state with an estimated decay rate of 80 fs puts the population to the first excited state (yellow arrow in Figure 2). This depicts mainly the intersystem crossing (ISC) in our model. The long-lived (first excited) state doubles as a representation of the Q-band and as a triplet state holding the population there. The triplet state has a time constant, which is outside of our observation window. In our model, the first excited state decays only by the exciton mechanism through which the excited population is returned to ground state.

The signal obtained by the amorphous sample is more complex. It seems that neither the rise nor the decrease of the signal can be described by the Lindblad equation with such a simplistic model. It was possible though to simulate the difference between the amorphous and crystalline signals. The difference can be fitted with a five-level model, just like before, with only a few modifications. One has to vary the eigenenergies to match the spectral features of the spin-coated sample. Then, the decay rate from the second to first excited state needs to be set to 50 fs. Lastly, a change in the exciton coupling strength and the dissipation rate by approximately an order of magnitude is necessary. All other excitation-related parameters were identical.

In Figure 5, results of the simulations overlaid with the data recorded for the liquid-deposited (blue) and spin-coated (orange) samples as well as the difference between them (green) are presented. The blue and green lines are the result

of the abovementioned simulations, while the orange line is the sum of the two (see the Supporting Information). This leads to the conclusion that the signal obtained from the spin-coated sample behaves as if there were two components in it: one similar to the liquid-deposited sample, dominated by the excitonic decay from neatly stacked MgPc molecules and one where the exciton coupling and dissipation rate are much higher, likely attributed to the close-packed formations (X-phase) that give rise to the NIR absorption peak. Both parameters indicate a structural change, which leads to tighter binding, higher dimensionality of the exciton dissipation mechanism, which in turn leads to faster decay. There was a good fit without having to change any excitation parameters, nor including any interaction effects between the two subsystems, which indicate no major interaction within the two subsystems present in the amorphous sample. In essence, from the scope of transient absorption, the amorphous sample behaves as a mix of two independent subsystems. This finding agrees with the results of the MIR study above where it was shown that there is a direct dimensionality difference in the decay mechanism between the both samples.

CONCLUSIONS

In summary, we demonstrated the transient dynamics taking place in the MIR spectral range for MgPc thin-film semiconductors of varying structural complexity. We performed a study of the dynamics of these samples within the visible range. Thereby, we were able to construct a simple and viable computational model for simulating the dynamics in high-quality MgPc thin films, at least in the scope of optical properties. In that, we demonstrated how the observed differences in the optical range can be traced back to structural differences of the samples and specifically a different exciton annihilation mechanism taking place and how this ties back to the effects observed in the MIR spectral range. The accuracy of the model can be improved by performing density functional theory calculations to obtain a better description of the molecular systems in terms of eigenenergies, dipole matrix, decay rates, and the nature of the states involved. All these can easily be used instead of the phenomenological matrices implemented here to enhance the quality of the results and the physical understanding of the system.

ASSOCIATED CONTENT

ⓈI Supporting Information

The Supporting Information is available free of charge at https://pubs.acs.org/doi/10.1021/acs.jpcc.1c04698.

> MIR transient absorption spectra and comparison with temperature-dependent FTIR spectra; MIR transient absorption spectra with parallel and perpendicular polarization schemes; temporal evolution comparison for the MIR transient absorption signal with parallel and perpendicular polarization schemes; transient absorption of MgPc solution in DMF; comparison between the GSB of liquid-deposited, spin-coated, and solution of MgPc in DMF; simulation and modeling results; and X-ray diffraction pattern of substrates and samples (PDF)

AUTHOR INFORMATION

Corresponding Authors

R. Kienberger − *Physik Department, Technische Universität München, Garching 85748, Germany;* Email: reinhard.kienberger@tum.de

H. Iglev − *Physik Department, Technische Universität München, Garching 85748, Germany;* ⓞ orcid.org/0000-0001-9208-0068; Email: higlev@ph.tum.de

Authors

D. Potamianos − *Physik Department, Technische Universität München, Garching 85748, Germany*

M. Nuber − *Physik Department, Technische Universität München, Garching 85748, Germany;* ⓞ orcid.org/0000-0002-4409-3590

A. Schletter − *Physik Department, Technische Universität München, Garching 85748, Germany*

M. Schnitzenbaumer − *Physik Department, Technische Universität München, Garching 85748, Germany*

M. Haimerl − *Physik Department, Technische Universität München, Garching 85748, Germany*

P. Scigalla − *Physik Department, Technische Universität München, Garching 85748, Germany*

M. Wörle − *Physik Department, Technische Universität München, Garching 85748, Germany*

L. I. Wagner − *Physik Department and Walter Schottky Institute, Technische Universität München, Garching 85748, Germany*

Complete contact information is available at:
https://pubs.acs.org/10.1021/acs.jpcc.1c04698

Notes

The authors declare no competing financial interest.

ACKNOWLEDGMENTS

REFERENCES

(1) Cook, M. J. Phthalocyanine thin films*. *Pure Appl. Chem* **1999**, *71*, 2145−2151.

(2) Hämäläinen, S. K.; Stepanova, M.; Drost, R.; Liljeroth, P.; Lahtinen, J.; Sainio, J. Self-assembly of cobalt-phthalocyanine molecules on epitaxial graphene on Ir(111). *J. Phys. Chem. C* **2012**, *116*, 20433−20437.

(3) Karimov, K. S.; Qazi, I.; Khan, T. A.; Draper, P. H.; Khalid, F. A.; Mahroof-Tahir, M. Humidity and illumination organic semiconductor copper phthalocyanine sensor for environmental monitoring. *Environ. Monit. Assess.* **2008**, *141*, 323−328.

(4) Hassan, S. S. M.; Kamel, A. H.; Elbehery, N. H. A. Potentiometric detection of low-levels of sulfamethazine in milk and pharmaceutical formulations using novel plastic membrane sensors. *J. Electrochem. Sci. Eng.* **2019**, *9*, 17−26.

(5) Boileau, N. T.; Cranston, R.; Mirka, B.; Melville, O. A.; Lessard, B. H. Metal phthalocyanine organic thin-film transistors: Changes in

electrical performance and stability in response to temperature and environment. *RSC Adv* **2019**, 9, 21478−21485.

(6) Ghosh, A. K.; Morel, D. L.; Feng, T.; Shaw, R. F.; Rowe, C. A. Photovoltaic and rectification properties of Al/ Mg phthalocyanine/ Ag Schottky-barrier cells. *J. Appl. Phys.* **1974**, 45, 230.

(7) Duong, T.; Peng, J.; Walter, D.; Xiang, J.; Shen, H.; Chugh, D.; Lockrey, M.; Zhong, D.; Li, J.; Weber, K.; et al. Perovskite solar cells employing copper phthalocyanine hole-transport material with an efficiency over 20% and excellent thermal stability. *ACS Energy Lett* **2018**, 3, 2441−2448.

(8) Blochwitz, J.; Pfeiffer, M.; Fritz, T.; Leo, K. Low voltage organic light emitting diodes featuring doped phthalocyanine as hole transport material. *Applied Physics Letters* **1998**, 73, 729−731.

(9) Jain, S.; Ridhi, R.; Soleimanioun, N.; Bharti, S.; Bhullar, G. K.; Tripathi, S. K. Layers dependent properties of magnesium phthalocyanine thin films prepared by Langmuir Blodgett method. *AIP Conf. Proc.* **2019**, 2093, 020041-1−020041-4.

(10) Valli, L. Phthalocyanine-based Langmuir-Blodgett films as chemical sensors. *Adv. Colloid and Interface Sci.* **2005**, 116, 13−44.

(11) Petty, M. C. *Langmuir-Blodgett Films*; Cambridge University Press: Cambridge, U.K., 1996.

(12) Komino, T.; Matsuda, M.; Tajima, H. The fabrication method of unsubstituted planar phthalocyanine thin films by a spin-coating technique. *Thin Solid Films* **2009**, 518, 688−691.

(13) Wang, B.; Zuo, X.; Wu, Y.; Chen, Z.; Li, Z. Preparation, characterization and gas sensing properties of high soluble metal (II) phthalocyanine thin films by spin-coating method. *Mater. Lett.* **2005**, 59, 3073−3077.

(14) Basova, T. V.; Kiselev, V. G.; Plyashkevich, V. A.; Cheblakov, P. B.; Latteyer, F.; Peisert, H.; Chassè, T. Orientation and morphology of chloroaluminum phthalocyanine films grown by vapor deposition: Electrical field-induced molecular alignment. *Chem. Phys.* **2011**, 380, 40−47.

(15) Mattox, D. M. *Handbook of Physical Vapor Deposition (PVD) Processing*; William Andrew/Elsevier: Boston, U.S.A., 2010.

(16) Hor, A. M.; Loutfy, R. O. Solvent-induced dimorphic transformation in magnesium phthalocyanine and its effect on the photoactivity. *Thin Solid Films* **1983**, 106, 291−301.

(17) Boguta, A.; Wróbel, D.; Bartczak, A.; Swietlik, R.; Stachowiak, Z.; Ion, R. M. Characterization of interfacial effects in organic macrocycles Langmuir and Langmuir-Blodgett layers studied by surface potential and FT-IR spectroscopy examination. *Mater. Sci. Eng. B Solid-State Mater. Adv. Technol.* **2004**, 113, 99−105.

(18) Endo, A.; Matsumoto, S.; Mizuguchi, J. Interpretation of the near-infrared absorption of magnesium phthalocyanine complexes in terms of exciton coupling effects. *J. Phys. Chem. A* **1999**, 103, 8193−8199.

(19) Valicsek, Z.; Horváth, O. Application of the electronic spectra of porphyrins for analytical purposes: The effects of metal ions and structural distortions. *Microchem. J.* **2013**, 107, 47−62.

(20) Schwieger, T.; Peisert, H.; Golden, M. S.; Knupfer, M.; Fink, J. Electronic structure of the organic semiconductor copper phthalocyanine and K-CuPc studied using photoemission spectroscopy. *Phys. Rev. B Condens. Matter Mater. Phys.* **2002**, 66, 1−5.

(21) Derkowska, B.; Wojdyła, M.; Czaplicki, R.; Bała, W.; Sahraoui, B. Influence of the central metal atom on the nonlinear optical properties of MPcs solutions and thin films. *Opt. Commun.* **2007**, 274, 206−212.

(22) Sakakibara, Y.; Bera, R. N.; Mizutani, T.; Ishida, K.; Tokumoto, M.; Tani, T. Photoluminescence properties of magnesium, chloroaluminum, bromoaluminum, and metal-free phthalocyanine solid films. *J. Phys. Chem. B* **2001**, 105, 1547−1553.

(23) Kamanina, N. V.; Denisyuk, I. Y. Optical Limiting of Near-IR Radiation in a System Based on Magnesium Phthalocyanine. *Opt. Spektrosc. (English Transl. Opt. i Spektrosk.* **2004**, 96, 77−80.

(24) Mi, J.; Guo, L.; Liu, Y.; Liu, W.; You, G.; Qian, S. Excited-state dynamics of magnesium phthalocyanine thin film. *Phys. Lett. A* **2003**, 310, 486−492.

(25) Ma, G.; Guo, L.; Mi, J.; Liu, Y.; Qian, S.; Pan, D.; Huang, Y. Femtosecond nonlinear optical response of metallophthalocyanine films. *Solid State Commun* **2001**, 118, 633−638.

(26) Seoudi, R.; El-Bahy, G. S.; El Sayed, Z. A. Ultraviolet and visible spectroscopic studies of phthalocyanine and its complexes thin films. *Opt. Mater.* **2006**, 29, 304−312.

(27) Critchley, S. M.; Willis, M. R.; Cook, M. J.; McMurdo, J.; Maruyama, Y. Deposition of ordered phthalocyanine films by spin coating. *J. Mater. Chem.* **1992**, 2, 157−159.

(28) Vasseur, K.; Broch, K.; Ayzner, A. L.; Rand, B. P.; Cheyns, D.; Frank, C.; Schreiber, F.; Toney, M. F.; Froyen, L.; Heremans, P. Controlling the texture and crystallinity of evaporated lead phthalocyanine thin films for near-infrared sensitive solar cells. *Appl. Mater. Interfaces* **2013**, 5, 8505−8515.

(29) Wang, Q.; Yang, F.; Zhang, Y.; Chen, M.; Zhang, X.; Lei, S.; Li, R.; Hu, W. Space-confined strategy toward large-area two-dimensional single crystals of molecular materials. *J. Am. Chem. Soc.* **2018**, 140, 5339−5342.

(30) Ran, G.; Wang, J.; Yue, J.; Pei, M.; Chen, J.; Zhang, W. Femtosecond excited state dynamics of liquid deposited magnesium phthalocyanine thin films. *Chem. Phys. Lett.* **2020**, 751, 137501.

(31) Mizuguchi, J.; Rihs, G.; Karfunkel, H. R. Solid-state spectra of titanylphthalocyanine as viewed from molecular distortion. *J. Phys. Chem.* **1995**, 99, 16217−16227.

(32) Hamui, L.; Sánchez-Vergara, M.; Sánchez-Ruiz, R.; Ruanova-Ferreiro, D.; Ballinas Indili, R.; Álvarez-Toledano, C. New development of membrane base optoelectronic devices. *Polymers* **2017**, 10, 16.

(33) Hütten, K.; Mittermair, M.; Stock, SO; Beerwerth, R.; Shirvanyan, V.; Riemensberger, J.; Duensing, A.; Heider, R.; Wagner, MS; Guggenmos, A.; et al. Ultrafast quantum control of ionization dynamics in krypton. *Nat. Commun.* **2018**, 9, 719−5.

(34) Uiberacker, M.; Uphues, T.; Schultze, M.; Verhoef, A. J.; Yakovlev, V.; Kling, M. F.; Rauschenberger, J.; Kabachnik, N. M.; Schröder, H.; Lezius, M.; et al. Attosecond real-time observation of electron tunnelling in atoms. *Nature* **2007**, 446, 627−632.

(35) Touka, N.; Benelmadjat, H.; Boudine, B.; Halimi, O.; Sebais, M. Copper phthalocyanine nanocrystals embedded into polymer host: Preparation and structural characterization. *J. Assoc. Arab Univ. Basic Appl. Sci.* **2013**, 13, 52−56.

(36) May, V. Kinetic theory of exciton-exciton annihilation. *J. Chem. Phys.* **2014**, 140, 054103.

(37) Johansson, J. R.; Nation, P. D.; Nori, F. An open-source Python framework for the dynamics of open quantum systems. *Comput. Phys. Commun.* **2012**, 183, 1760−1772.

(38) Johansson, J. R.; Nation, P. D.; Nori, F. QuTiP 2: A Python framework for the dynamics of open quantum systems. *Comput. Phys. Commun.* **2013**, 184, 1234−1240.

(39) Cha, S.; Sung, J. H.; Sim, S.; Park, J.; Heo, H.; Jo, M.; Choi, H. 1s-intraexcitonic dynamics in monolayer MoS2 probed by ultrafast mid-infrared spectroscopy. *Nat. Commun.* **2016**, 7, 1−7.

(40) Yanagisawa, S.; Yamauchi, K.; Inaoka, T.; Oguchi, T.; Hamada, I. Origin of the band dispersion in a metal phthalocyanine crystal. *Phys. Rev. B* **2014**, 90, 245141.

(41) Norton, J. E.; Brédas, J. L. Theoretical characterization of titanyl phthalocyanine as a -type organic semiconductor: Short intermolecular interactions yield large electronic couplings and hole transport bandwidths. *J. Chem. Phys.* **2008**, 128, 1228.

(42) Schwarze, M.; Tress, W.; Beyer, B.; Gao, F.; Scholz, R.; Poelking, C.; Ortstein, K.; Günther, A. A.; Kasemann, D.; Andrienko, D.; et al. Band structure engineering in organic semiconductors. *Science* **2016**, 352, 1446−1449.

(43) Ortí, E.; Brédas, J. L.; Clarisse, C. Electronic structure of phthalocyanines: Theoretical investigation of the optical properties of phthalocyanine monomers, dimers, and crystals. *J. Chem. Phys.* **1990**, 92, 1228−1235.

(44) Zhang, X.; Zhang, Y.; Jiang, J. Towards clarifying the N-M vibrational nature of metallo-phthalocyanines: Infrared spectrum of phthalocyanine magnesium complex: Density functional calculations.

Spectrochim. Acta—Part A Mol. Biomol. Spectrosc. **2004**, *60*, 2195–2200.

(45) Zhao, S.; He, D.; He, J.; Zhang, X.; Yi, L.; Wang, Y.; Zhao, H. Probing excitons in transition metal dichalcogenides by Drude-like exciton intraband absorption. *Nanoscale* **2018**, *10*, 9538–9546.

(46) Gulbinas, V.; Chachisvilis, M.; Persson, A.; Sundstroem, V.; Svanberg, S. Ultrafast excitation relaxation in colloidal particles of chloroaluminum phthalocyanine: one-dimensional exciton-exciton annihilation. *J. Phys. Chem* **1994**, *98*, 8118–8123.